Effect of temperature gradient locally applied on a long horizontal cavity

G. P. Extremet, P. Bontoux and B. Roux*

A numerical study of buoyancy-driven gas flow in long horizontal cavities, with $Pr=0.73$, was made with reference to the case of local application of a horizontal temperature gradient. Such a situation is relevant to crystal growth in two-zone furnaces. The effect of the width of the external temperature gradient on the main properties of the flow (velocity profiles, isotherm and streamline patterns) was examined for Grashof numbers ranging from the conduction regime up to the beginning of the boundary layer regime. An attempt was made to correlate the values of the maximum velocity with the aspect ratio of the cavity and the width of the external temperature gradient.

Keywords: *buoyancy-driven gas flow, numerical simulation, finite difference methods, two-zone furnaces, local temperature gradient, long horizontal cavity*

Introduction

We consider natural convection developing in long horizontal cavities subjected to a locally applied horizontal temperature gradient. Such a situation appears in crystal growth from vapour transport in a closed ampoule placed in a furnance which is designed to deliver two large isothermal zones (the hot one, at T_2, on the source side, and the cold one, at T_1, on the crystal side) separated by an abrupt temperature gradient. There has, until now, been a complete lack of data on flow characteristics for crystal growth in such systems. Indeed, all the previous analytical and numerical hydrodynamic studies devoted to crystal growth systems in long horizontal ampoules have been limited to the case where the horizontal temperature gradient is uniformly applied along the entire ampoule.

In such simpler systems, called one-gradient models (abbreviated 1G), a flow regime classification is now rather well established (depending on Grashof number Gr) between the conduction regime for low Gr and the intermediate and boundary layer regimes for higher Gr[1,2]. Analytical solutions have been obtained for low Gr for two-dimensional and cylindrical cavities[3–8]. The basic feature of such solutions is direct association of a dynamic field to the temperature gradient in the centre of the cavity. For the conduction regime the isotherms are vertical in most of the cavity, the temperature gradient being everywhere the same as the external gradient imposed. For higher Gr the flow modifies the temperature pattern, but the temperature gradient in the centre has been expressed in power laws of aspect ratio and Gr, obtained by correlating results of direct numerical simulation.

For the two-zone furnace (abbreviated 2Z), in general the temperature variation in the flow is not uniform, even for small Gr. The aim of the work described in this paper was to derive some empirical laws (through direct numerical simulation) expressing the temperature gradient in the centre of the cavity in terms of the aspect ratio of the cavity and the width of the external temperature gradient imposed by the furnace. A second goal was to ascertain if the dynamic field (mainly the maximum horizontal velocity) could be directly connected to this internal temperature gradient.

The computations carried out in the present study were limited to $Pr=0.73$.

Physical and mathematical model

A two-dimensional model was chosen for the analysis of the main features of the flow in the vertical plane of a growth ampoule in a 2Z furnace system.

Geometry and physical model

We consider the flow in a rectangular domain, as shown in Fig 1. This domain is bounded by vertical and horizontal walls respectively of lengths H and L, with aspect ratio $l=H/L$. The vertical walls are maintained at constant but different temperatures T_2 and T_1. The temperature profile is the same along both the horizontal walls. It varies linearly in y on the interval $[\bar{y}_1, L-\bar{y}_1]$ centred at $\bar{y}=L/2$. The width $L_{\Delta T}=L-2\bar{y}_1$ of the imposed (external) temperature gradient is a specific parameter of the study. When $L_{\Delta T}=L$, we obtain the simpler 1G model considered in the analysis of Bontoux *et al*[9].

Governing equations

The dependent primitive variables are the velocities $\bar{u}$ and $\bar{v}$, and the temperature T. The density ρ is directly connected to T through the Boussinesq approximation as follows:

$$\rho=\rho_0[1-\hat{\beta}(T-T_0)] \tag{1}$$

where the subscript 0 refers to reference conditions, and the coefficient of thermal expansion is expressed as

$$\hat{\beta}=\frac{1}{T_0} \text{ with } T_0=\frac{1}{2}(T_1+T_2)$$

The governing system is given by the Navier–Stokes and energy equations, the scales for the dimensionless variables are

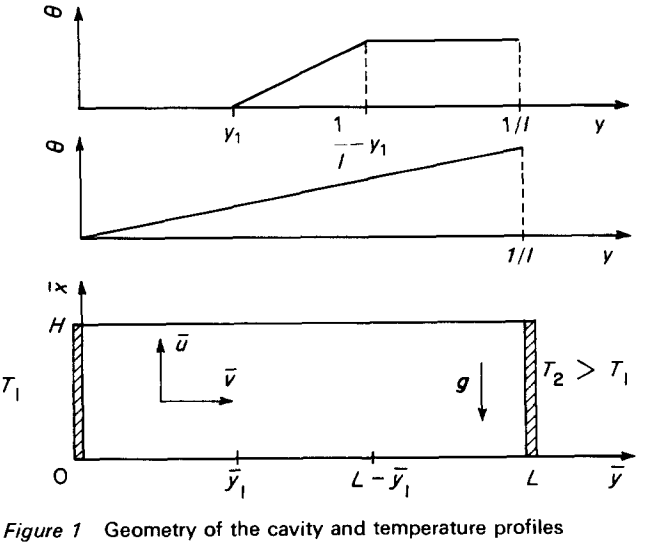

Figure 1 Geometry of the cavity and temperature profiles

*I.M.F.M., 1 rue Honnorat, 13003 Marseille, France

0142-727X/87/010026-11$3.00

respectively H and v/H for the length and the velocity, while the temperature is defined as

$$\theta=(T-T_0)/\Delta T$$

When the vorticity and the steam-function are taken as dependent variables, the resulting governing system is written as follows:

$$\frac{\partial\zeta}{\partial t}+u\frac{\partial\zeta}{\partial x}+v\frac{\partial\zeta}{\partial y}=\frac{\partial^2\zeta}{\partial x^2}+\frac{\partial^2\zeta}{\partial y^2}+Gr\frac{\partial\theta}{\partial y} \tag{2}$$

$$\frac{\partial^2\psi}{\partial x^2}+\frac{\partial^2\psi}{\partial y^2}=\zeta \tag{3}$$

$$Pr\left(\frac{\partial\theta}{\partial t}+u\frac{\partial\theta}{\partial x}+v\frac{\partial\theta}{\partial y}\right)=\frac{\partial^2\theta}{\partial x^2}+\frac{\partial^2\theta}{\partial y^2} \tag{4}$$

where

$$u=\frac{\partial\psi}{\partial y}\text{ and }v=-\frac{\partial\psi}{\partial x} \tag{5}$$

As usual, the basic dimensionless parameters are the Grashof and the Prandlt numbers:

$$Gr=\hat{\beta}g\Delta TH^3/v^2$$

and

$$Pr=v/\kappa$$

The problem involves two additional parameters, the aspect ratio of the cavity, l, and the reduced width of the external temperature gradient, $\gamma=L_{\Delta T}/L$.

Boundary conditions

The dynamic boundary conditions on the walls are assumed to be the natural no-slip and no-permeability conditions:

$$\psi_w=\left(\frac{\partial\psi}{\partial n}\right)_w=0 \tag{6}$$

where n is the normal to the wall.

The thermal conditions are

(i) at the vertical walls,

$$\theta_w(x,0)=-\frac{1}{2}\text{ and }\theta_w\left(x,\frac{1}{l}\right)=\frac{1}{2} \tag{7}$$

(ii) along the horizontal walls,

$$\theta_w(0,y)=\theta_w(1,y)=-\frac{1}{2}+\Theta(y) \tag{8}$$

with

$$\Theta(y)=0\text{ for }0\leqslant y\leqslant y_1$$

$$\Theta(y)=(y-y_1)\frac{l}{\gamma}\text{ for }y_1\leqslant y\leqslant\left(\frac{1}{l}-y_1\right)$$

$$\Theta(y)=1\text{ for }\left(\frac{1}{l}-y_1\right)\leqslant y\leqslant\frac{1}{l}$$

Note that γ is related to y_1 by: $\gamma=1-2y_1l$.

The boundary conditions on the vorticity are derived from the numerical approximation of the equation

$$\zeta_w=\left(\frac{\partial^2\psi}{\partial n^2}\right)_w \tag{9}$$

the discretized formulation of which is given below.

Analytical flow solutions ($\gamma=1$, $l\to0$)

For $\gamma=1$ (the 1G thermal model), analytical flow solutions have been proposed[3-6] for the core of shallow cavities ($l\ll1$). These solutions are based on power series expansion of $a=Gr\,(\partial\theta/\partial y)_m$, with the assumption that the velocity is independent of the horizontal direction y, the convective terms are small, and the temperature gradient in the core, $(\partial\theta/\partial y)_m$, is constant. A parallel flow solution is then derived from the first-order terms

Notation

a	Constant in Eqs (10) and (11)
c	Constant in Eq (17)
g	Gravitational acceleration
Gr	Grashof number $\equiv\hat{\beta}g\Delta TH^3/v^2$
h	Spatial step size
H	Height of the cavity
l	Aspect ratio $\equiv H/L$
L	Length of the cavity
$L_{\Delta T}$	Width of the temperature gradient
n	Variable normal to the wall
Pr	Prandtl number $\equiv v/\kappa$
t	Time variable
T_0	Reference temperature
T_1, T_2	Temperatures on the vertical walls, cold and hot
$\bar{u}$, $\bar{v}$	Components of the local velocity
u, v	Dimensionless components of velocity $\equiv \bar{u}H/v$, $\bar{v}H/v$
$\tilde{u}$, $\tilde{v}$	Dimensionless components of velocity $\equiv u/l$, v/l
v_{max}	Analytical expression for velocity v (Eq (20))
$v_{i,max}$	Analytical expression for velocity v (Eqs (21) and (22))
$v_{max,c}$	Computed value for velocity v
$\bar{x}$, $\bar{y}$	Cartesian coordinates (Fig 1)
x, y	Dimensionless cartesian coordinates $\equiv x/H$, y/L
$\tilde{y}$	Dimensionless cartesian coordinate $\equiv ly$
y_1	Abscissa defining the gradient width
α_ψ, α_θ	Relaxation factors
$\hat{\beta}$	Thermal expansion coefficient
β	Parameter defined as $\tilde{v}_{max,c}/\tilde{v}_{max}$
γ	Reduced width of the external temperature gradient $\equiv L_{\Delta T}/L$
$(\partial\theta/\partial y)$	Horizontal temperature gradient
ΔT	Temperature difference $\equiv T_2-T_1$
ε	Matching function in Eq (17)
ζ	Vorticity
θ	Dimensionless temperature $\equiv(T-T_0)/\Delta T$
$\Theta(y)$	Horizontal temperature function in Eq (8)
κ	Thermal diffusivity
v	Kinematic viscosity
ρ, ρ_0	Density variables in Eq (1)
ψ	Stream-function

Subscripts

0	Reference conditions
w, w−1	Values on the walls, and near the walls, respectively
m	Values in the middle of the cavity
max	Maximum values
c	Computed values

Superscipts

n, $n+1$	Steps in the ADI scheme
*	Virtual intermediate step in the ADI scheme

as follows:

$$\psi(x) = -ax^2(x-1)^2/24 \tag{10}$$

and

$$v(x) = ax(2x-1)(x-1)/12 \tag{11}$$

This corresponds to two counter-flows coming from the hot boundary, above, and from the cold one, below. At low Grashof numbers, the horizontal gradient $(\partial\theta/\partial y)_m$ is constant in the core and generates the main buoyancy forces. This corresponds to the core-driven regime described by Cormack *et al*[1,10] and Imberger[11]. At large Grashof numbers, the main buoyancy forces are located in the end regions (boundary layer regime), but functional laws for the variation of $(\partial\theta/\partial y)_m$ are available[1,6,12] and allow approximation of the flow profiles with Eqs (10) and (11).

Numerical approximation

Numerical schemes

The numerical solution of the differential system, Eqs (2)–(5), is made with a hermitian finite difference method, based on a fourth-order accurate scheme for the Poisson equation and a classical second-order accurate scheme for the transport equations[13–15]. The relation of Hirsh gives a third-order approximation for the vorticity at the boundaries:

$$\zeta_w = \frac{12}{h^2}(\psi_{w-1} - \psi_w) + \frac{6}{h}\left\{\left(\frac{\partial\psi}{\partial n}\right)_w + \left(\frac{\partial\psi}{\partial n}\right)_{w-1}\right\} + \left(\frac{\partial^2\psi}{\partial n^2}\right)_{w-1} + 0(h^3) \tag{12}$$

where h is the spatial step size and $(w-1)$ refers to the first internal point close to the boundary.

As proposed by Mallinson and De Vahl Davis[16], convergence towards steady state solution is sought with the false transient method, for the transport equations in ζ and θ, and for the Poisson equation in ψ, at which a fictitious time derivative term $(1/\alpha_\psi)(\partial\psi/\partial t)$ is added. The finite difference system is solved by a classical ADI method:

$$Pr\left[\frac{2}{\alpha_\theta \Delta t}(\theta^* - \theta^n) + u\left(\frac{\partial\theta}{\partial x}\right)^n + v\left(\frac{\partial\theta}{\partial y}\right)^*\right] = \left(\frac{\partial^2\theta}{\partial x^2}\right)^n + \left(\frac{\partial^2\theta}{\partial y^2}\right)^* \tag{13a}$$

$$Pr\left[\frac{2}{\alpha_\theta \Delta t}(\theta^{n+1} - \theta^*) + u\left(\frac{\partial\theta}{\partial x}\right)^{n+1} + v\left(\frac{\partial\theta}{\partial y}\right)^*\right] = \left(\frac{\partial^2\theta}{\partial x^2}\right)^{n+1} + \left(\frac{\partial^2\theta}{\partial y^2}\right)^* \tag{13b}$$

$$\frac{2}{\Delta t}(\zeta^* - \zeta^n) + u\left(\frac{\partial\zeta}{\partial x}\right)^n + v\left(\frac{\partial\zeta}{\partial y}\right)^* = \left(\frac{\partial^2\zeta}{\partial x^2}\right)^n + \left(\frac{\partial^2\zeta}{\partial y^2}\right)^* + Gr\left(\frac{\partial\theta}{\partial y}\right)^{n+1} \tag{14a}$$

$$\frac{2}{\Delta t}(\zeta^{n+1} - \zeta^*) + u\left(\frac{\partial\zeta}{\partial x}\right)^{n+1} + v\left(\frac{\partial\zeta}{\partial y}\right)^* = \left(\frac{\partial^2\zeta}{\partial x^2}\right)^{n+1} + \left(\frac{\partial^2\zeta}{\partial y^2}\right)^* + Gr\left(\frac{\partial\theta}{\partial y}\right)^{n+1} \tag{14b}$$

$$\frac{2}{\alpha_\psi \Delta t}(\psi^* - \psi^n) = \left(\frac{\partial^2\psi}{\partial x^2}\right)^n + \left(\frac{\partial^2\psi}{\partial y^2}\right)^* - \zeta^{n+1} \tag{15a}$$

$$\frac{2}{\alpha_\psi \Delta t}(\psi^{n+1} - \psi^*) = \left(\frac{\partial^2\psi}{\partial x^2}\right)^{n+1} + \left(\frac{\partial^2\psi}{\partial y^2}\right)^* - \zeta^{n+1} \tag{15b}$$

where α_ψ and α_θ are relaxation factors which are chosen to accelerate the convergence. The velocities u and v appearing in the convective terms are expressed at the step n. The stability conditions of the algorithm were theoretically and numerically studied for the natural convection problem by Bontoux *et al*[17]. A relation for the critical step size is derived from the stability analysis as follows:

$$\frac{\Delta t_c}{h^2} \approx \frac{1 + \{1 + (28/Pr)\}^{1/2}}{7} Pr \tag{16}$$

Optimization and initial conditions

The general method was optimized for use on the vector computer Cray-1S. Substantial gains were obtained in computing time by the vectorization of the algorithms[18,19] and the general use of vectorized program libraries (SCILIB), Cray Scientific Library). With 21×81 mesh points, a convergent solution was obtained with 233 iterations. The computing times were: 78.23 s on a Cyber 750; 14.17 and 3.15 on a Cray-1S before and after vectorization, respectively.

The analytical solutions, Eqs (10) and (11), were used with $a = Gr$ for the initialization of the computation. Expressions for the vertical component of the velocity and the temperature were derived from the second-order terms of the expansions in $Gr(\partial\theta/\partial y)_m$ given by Bejan and Tien[6]. As the enclosure had a finite aspect ratio, the solutions were adjusted by a matching function $\varepsilon(y)$ which ensured the non-permeability condition at the vertical boundaries. The function $\varepsilon(y)$ was chosen as a hyperbolic tangent of a fourth-order polynomial, the constants of which were empirically determined in order to match the analytical solutions, Eqs (10) and (11), in the core and to represent the turn of the flow in the end regions:

$$\varepsilon(y) = \tanh\left[cy^2\left(\frac{1}{l} - y\right)^2\right] \tag{17}$$

The value for constant c in Eq (17) was determined as $c \approx 3.27l^2/(1-l)^2$ to match the core solution[20] at $y = 1$. Two meshes were considered for the present study: 21×41 and 21×81; the corresponding numerical parameters were respectively

$$l^2\Delta t = 5.5 \times 10^{-5},\quad \alpha_\psi = 1,\quad \alpha_\theta = 75$$

and

$$l^2\Delta t = 7.3 \times 10^{-5},\quad \alpha_\psi = 1,\quad \alpha_\theta = 10$$

Results in the conducting regime (low *Gr*)

The ability or limitation of the analytical solutions to approximate the main features of the flow in the core of rectangular and cylindrical enclosures have been discussed elsewhere with respect to experiments and computations in the case of a simple 1G model[9]. In the work reported here we attempted to extend the derivation of empirical laws on the basis of numerical simulation for conduction-dominated regimes in a rectangular cavity and for a 2Z furnace. The goal was to evaluate the temperature gradient $(\partial\theta/\partial y)_m$ and to establish its dependency on the aspect parameters l and γ.

Influence of γ and l on isotherm and streamline patterns

Typical flow solutions at fixed Gr and l are given in Figs 2, 3 and 4 for $l = 0.10$, 0.25 and 0.50, respectively, with γ ranging from 0.05 to 1.0. The isotherm patterns are characteristic of conduction. The convective cells they generate develop differently with γ, depending on the aspect ratio l. When l is small ($l = 0.1$ in Fig 2), the convective cell is very concentrated near the centre at $\gamma = 0.05$, and spreads to the entire domain when $\gamma \geqslant 0.75$. At moderate aspect ratios ($l = 0.25$ in Fig 3) the basic cell at $\gamma \geqslant 0.2$ is mainly 'cat-eye' shaped. Although the temperature gradient is located at the centre domain, it drives the convective flow all around; the streamlines generated in the core irrigating the vertical boundaries. At larger gradient width, $\gamma \geqslant 0.5$, the flow pattern corresponds to a more regular cell

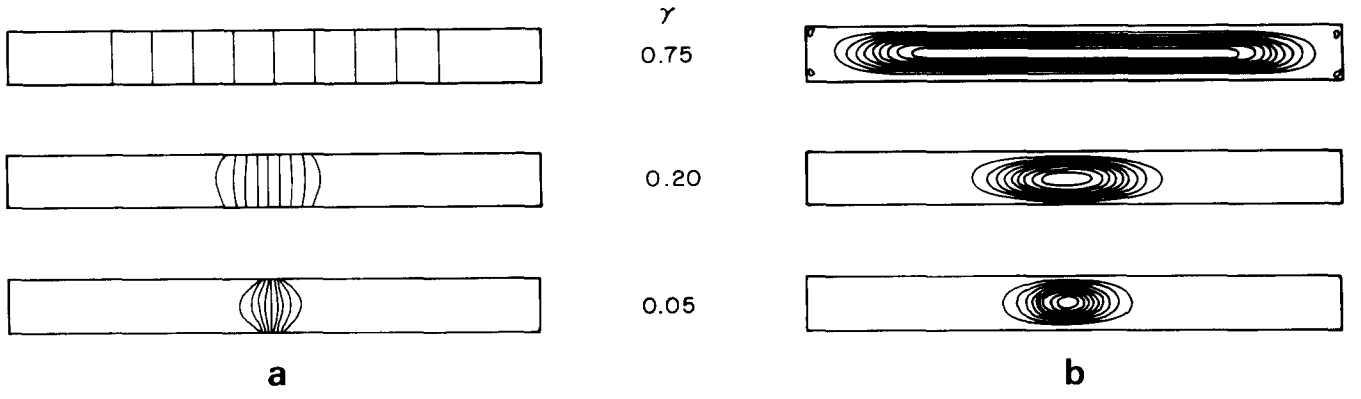

Figure 2 2Z model: (a) isotherm patterns ($T_i=(i-4)/10$, $i=0$ to 8), and (b) streamline patterns ($\psi_i=i/10$, ψ_{max}, $i=1$ to 9) for $Gr\approx 0.420$ and $l=0.10$ at $\gamma=0.05$ ($\psi_{max}=-7.51\times10^{-4}$), 0.20 ($\psi_{max}=-4.56\times10^{-4}$) and 0.75 ($\psi_{max}=-1.38\times10^{-4}$)

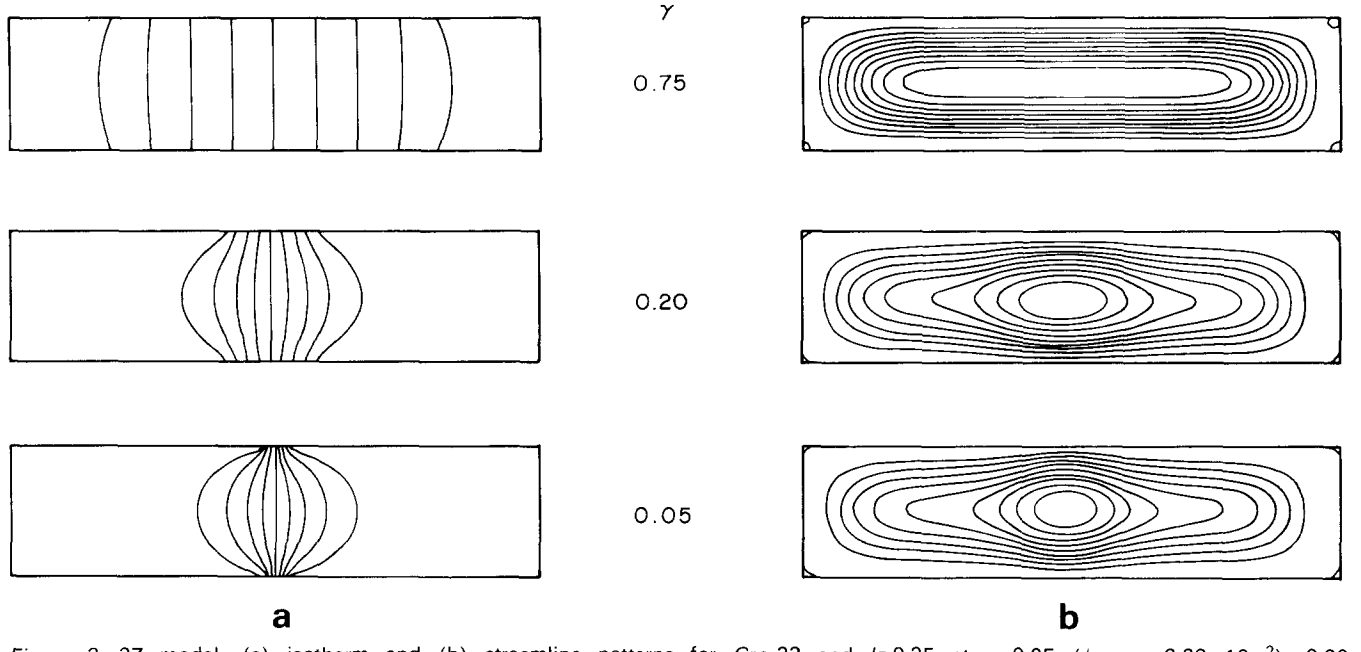

Figure 3 2Z model: (a) isotherm and (b) streamline patterns for $Gr\approx 22$ and $l=0.25$ at $\gamma=0.05$ ($\psi_{max}=-2.23\times10^{-2}$), 0.20 ($\psi_{max}=-2.03\times10^{-2}$) and 0.75 ($\psi_{max}=1.48\times10^{-2}$)

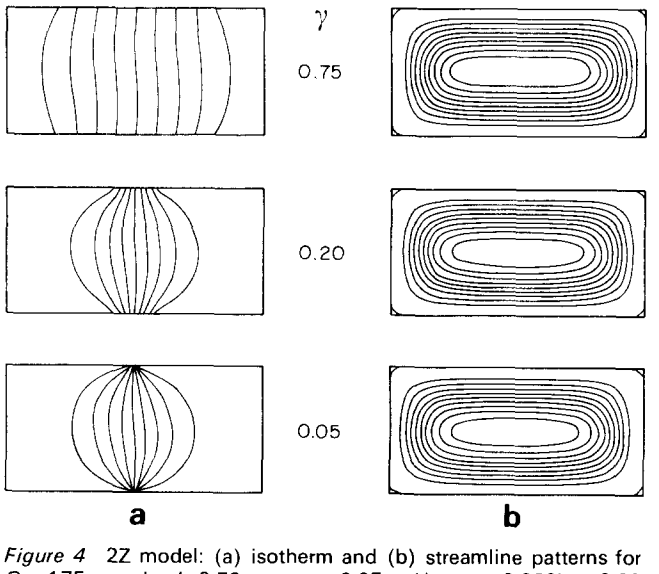

Figure 4 2Z model: (a) isotherm and (b) streamline patterns for $Gr\approx 175$ and $l=0.50$ at $\gamma=0.05$ ($\psi_{max}=-0.230$), 0.20 ($\psi_{max}=-0.228$) and 0.75 ($\psi_{max}=-0.223$)

occupying all the cavity and similar to the basic unicell of the classical 1G model ($\gamma=1$). When l is larger ($l=0.5$ in Fig 4) the structure of the streamline pattern remains unaffected by the variation of γ.

Influence of γ and l on the main flow properties

In addition to these results, the temperature profiles along horizontals at various heights in the cavity (including the wall and the centre line) are shown in Fig 5 for the same l and γ, with the temperature gradient along the horizontal centre line. Except at $\gamma=1$, where the gradient is constant ($\partial\theta/\partial y=l$) through the entire cavity, the temperature gradient on the centre line is maximum at the middle of the wall gradient zone, and tends towards zero at the side walls.

As the analytical solution assumes constant $(\partial\theta/\partial y)_m$ and parallel flow in the core of the gradient zone, it might seem that the field of application should be limited approximatively to the case of $\gamma/l>1$. However, on the basis that the computed solutions exhibit S-shaped profiles, as with Eq (11) (Fig 6), the extension of the analytical solutions is also analysed at $\gamma/l<1$.

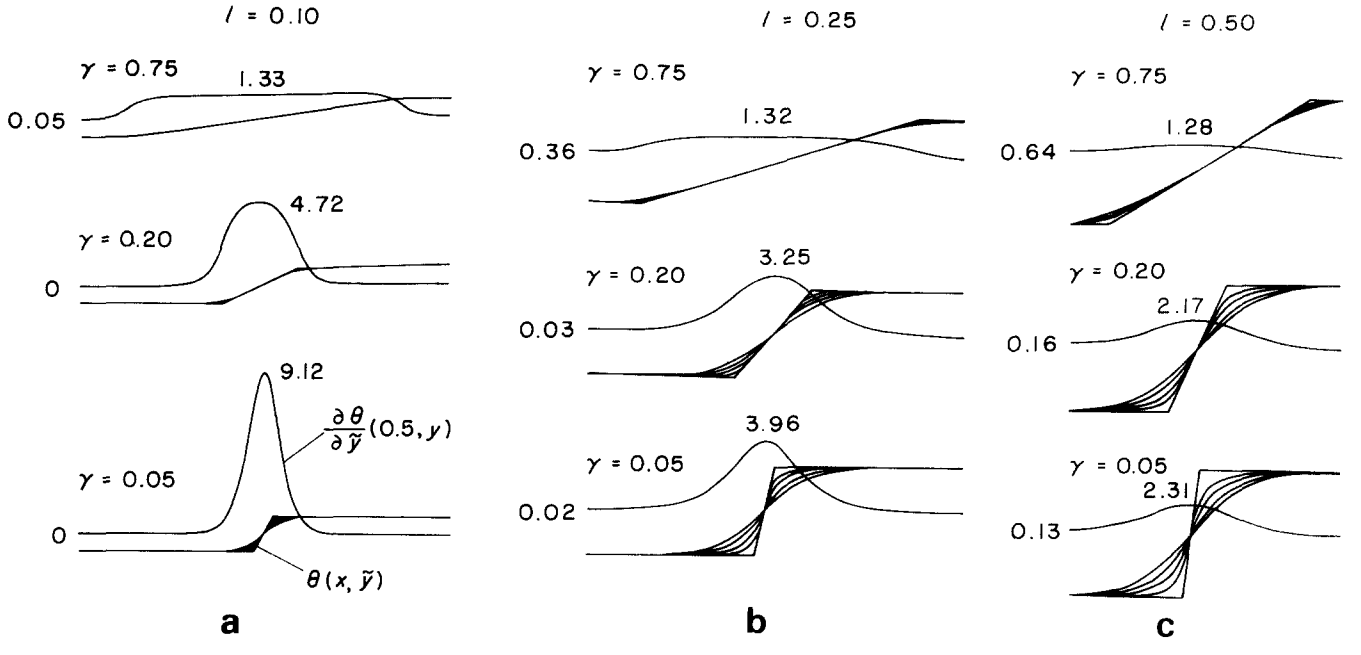

Figure 5 2Z model: temperature gradient ($\partial\theta/\partial\tilde{y}$) along the horizontal axis of the cavity and temperature profiles at various heights $x=0.0, 0.1, 0.2, 0.3, 0.4, 0.5$ for (a) $Gr=0.420$, $l=0.1$, (b) $Gr/l^3\approx1430$, $l=0.25$, and (c) $l=0.50$, at various values of γ

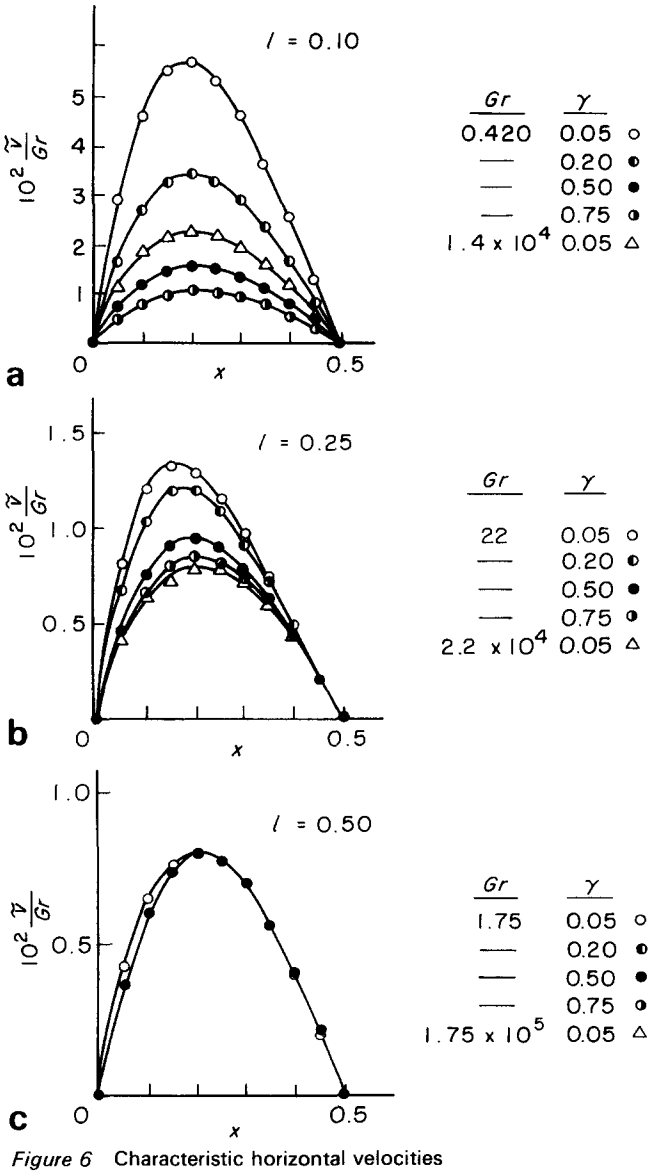

Figure 6 Characteristic horizontal velocities

Analysis of the results in the conducting regime

Influence of γ and l on $(\partial\theta/\partial y)_m$ (or $(\partial\theta/\partial\tilde{y})_m$)

The basic parameter entering in the solution Eq (11) is $(\partial\theta/\partial y)_m$. The computed values of $(\partial\theta/\partial\tilde{y})_m$ in the middle of the gradient zone are reported in Table 1 for a range of aspect ratios and gradient widths, $0.10\leqslant l\leqslant0.50$ and $0.05\leqslant\gamma\leqslant1.0$. These results obtained in the conducting regime ($Gr/l^3=420$ and 1420) are shown in Fig 7 and can be correlated with the two following functional laws:

$$l\left(\frac{\partial\theta}{\partial\tilde{y}}\right)_m\approx1 \quad \text{when } \frac{\gamma}{l}<1 \tag{18}$$

$$\gamma\left(\frac{\partial\theta}{\partial\tilde{y}}\right)_m\approx1 \text{ when } \frac{\gamma}{l}>1 \tag{19}$$

where $\tilde{y}=ly$.

Analysis of the results in terms of v_{max} (or $\tilde{v}_{max}$)

From Eq (11), the analytical expression for the maximum velocity, which occurs at $x=1/2(1\pm1/\sqrt{3})$, is as follows:

$$v_{max}=\frac{Gr}{72\sqrt{3}}\left(\frac{\partial\theta}{\partial y}\right)_m \tag{20}$$

In fact, we will consider a velocity renormalized by the length L, $\tilde{v}=v/l$ and thus:

$$\tilde{v}_{max}=\frac{Gr}{72\sqrt{3}}\left(\frac{\partial\theta}{\partial\tilde{y}}\right)_m$$

With the functional laws of Eqs (18) and (19) for $(\partial\theta/\partial\tilde{y})_m$, two expressions are derived from Eq (20), respectively:

$$v_{1,max}=\frac{Gr}{72\sqrt{3}} \text{ or } \tilde{v}_{1,max}=\frac{Gr}{72\sqrt{3}l} \quad \text{when } \frac{\gamma}{l}<1 \tag{21}$$

$$v_{2,max}=\frac{Gr}{72\sqrt{3}}\frac{l}{\gamma} \text{ or } \tilde{v}_{2,max}=\frac{Gr}{72\sqrt{3}\gamma} \quad \text{when } \frac{\gamma}{l}>1 \tag{22}$$

Table 1 Solutions for $(\partial\theta/\partial\tilde{y})$ in terms of the aspect ratio l and the gradient ratio γ (conduction regime)

l \ γ	0.05	0.10	0.20	0.50	0.75	1.00
0.10	9.124	7.375	4.719	1.999	1.333	1.000
0.15	6.404	5.705	4.215	1.986	1.333	—
0.20	4.895	4.562	3.695	1.950	1.329	1.000
0.25	3.962	3.781	3.247	1.896	1.321	—
0.50	2.312	2.283	2.174	1.666	1.276	1.000

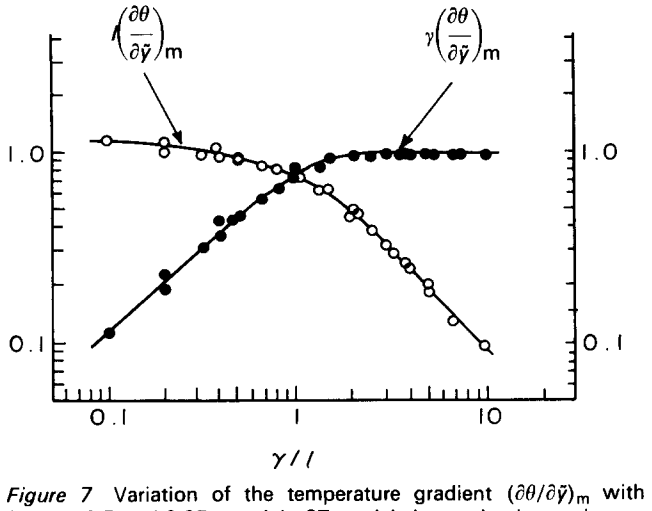

Figure 7 Variation of the temperature gradient $(\partial\theta/\partial\tilde{y})_m$ with $0.1<l<0.5$ and $0.05<\gamma<1$ in 2Z models in conduction regimes

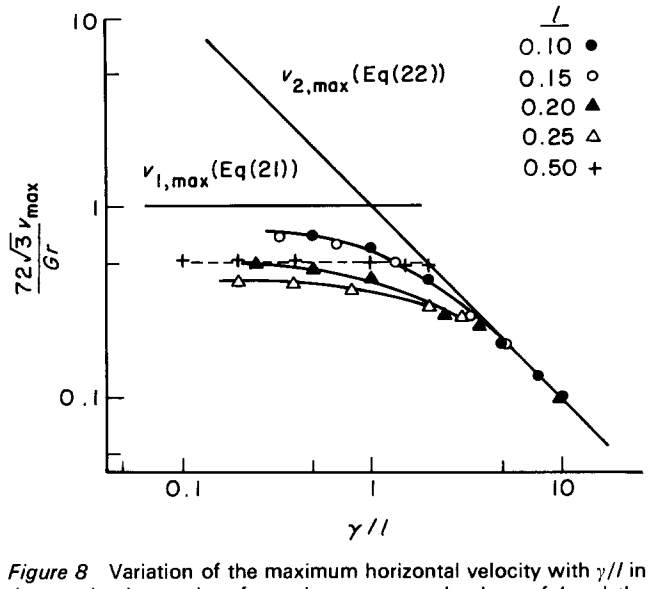

Figure 8 Variation of the maximum horizontal velocity with γ/l in the conduction regime for various computed values of l and the analytical laws of Eqs (21) and (22)

Considering a new variable defined as $72\sqrt{3}v_{max}/Gr$, Eqs (21) and (22) can be represented as two straight lines in terms of γ/l (Fig 8); these two lines interest at $\gamma=l$. The computed data in Table 2 are displayed also in Fig 8 and agree with the behaviour predicted by Eqs (21) and (22). In the domain $\gamma/l>1$, the agreement becomes better as γ/l increases, for which $72\sqrt{3}v_{max}/Gr$ is nearly proportional to l/γ. It is mostly qualitative when $\gamma/l<1$, because, as predicted by Eq (21), $72\sqrt{3}v_{max}/Gr$ becomes independent of γ/l but converges towards values which depend on l, and, anyway, stays below the theoretical value of 1.

These behaviour patterns can be interpreted as follows.

(i) When γ is decreased from 1 to 0.05 at constant ΔT and l, but in such a way that $\gamma>l$, the wall temperature gradient is locally increased, and is the gradient in the fluid (Figs 2 and 4); but the temperature gradient remains almost the same at the wall and in the core. The computed values of v_{max} are well predicted by Eq (22) as being proportional to $1/\gamma$ at a given l.

(ii) When $\gamma<l$ the temperature gradient strongly varies from the wall to the core, where it takes a much smaller values due to the low conductivity of gases (Figs 2 and 4). In addition, it strongly diminishes outside the external temperature gradient zone in the longitudinal direction (Fig 5), although the profiles $v(x)$ are almost independent of y over a much larger domain (Fig 4). We would have to take some mean values of $(\partial\theta/\partial y)_m$ over such a domain to limit the overprediction given by Eq (21).

It is to be noted, however, that the overprediction of the horizontal velocity is maximal when $l=0.25$ (the 'cat-eye' situations in Fig 3), while the centre gradient drives the flow also in the lateral regions near the vertical walls. At $l=0.50$, the magnitude of the velocity is quite independent of γ in the range $0.05\leqslant\gamma\leqslant0.50$ (Figs 6 and 8).

The limitation of Eq (21) is also exhibited when relating the computed maximum of v, $\tilde{v}_{max,c}$, and $(\partial\theta/\partial\tilde{y})_m$ (given in Tables 2 and 1). This maximum is scaled by β, defined as $\tilde{v}_{max,c}/\tilde{v}_{max}$. The values of β are plotted in terms of γ for various values of l in Fig 9. The extrema of β are: 1 at $l=\gamma=1$; and nearly 0.43 when $\gamma=0.05$, and $0.25<l<0.50$. The main features of the results presented in Fig 9 can be summarized as follows:

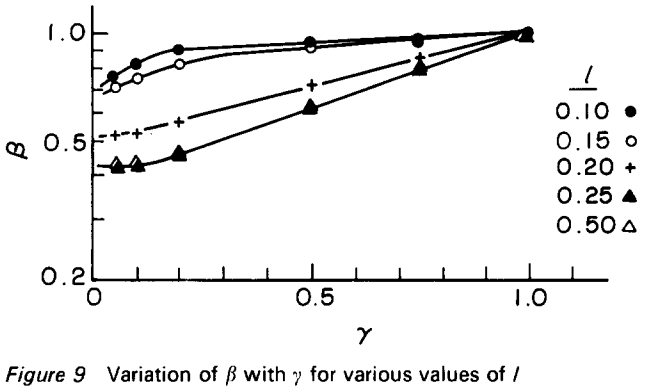

Figure 9 Variation of β with γ for various values of l

Table 2 Solutions for the maximum horizontal velocity component $\tilde{v}_{max,c}$ for various l and γ and conduction regimes

l \ γ	0.05	0.10	0.20	0.50	0.75	1.00	*Gr*
0.10	0.016 95	0.014 80	0.010 30	0.004 57	0.003 12	0.002 39	0.4
0.15	0.124 0	0.116 1	0.093 74	0.048 77	0.034 35	—	4.8
0.20	0.159 2	0.152 2	0.132 8	0.088 46	0.072 37	0.064 01	11.4
0.25	0.207 1	0.197 1	0.184 4	0.147 4	0.132 8	—	22.3
0.50	1.007	1.008	1.009	1.004	1.000	0.997 7	178.6

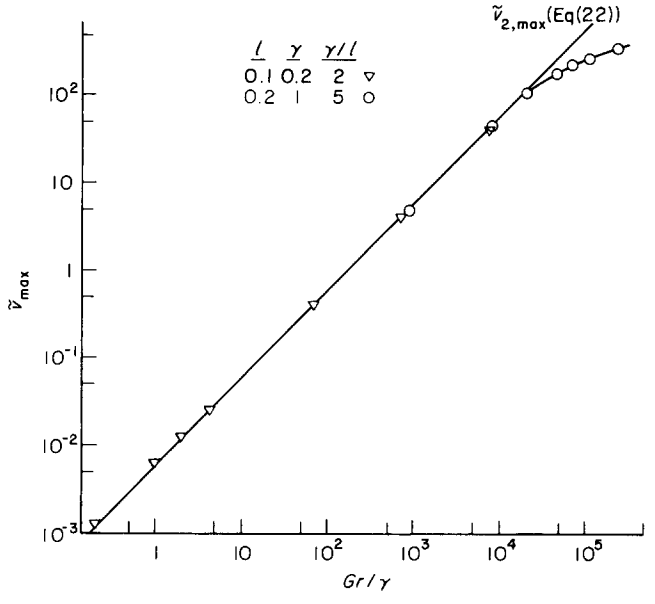

Figure 10 Variation of the maximum horizontal velocity in the middle of the gradient zone with Gr/γ for various values of l and γ (analytical $\tilde{v}_{2,max}$ and computed solutions $\tilde{v}_{max,c}$ for $\gamma/l>1$)

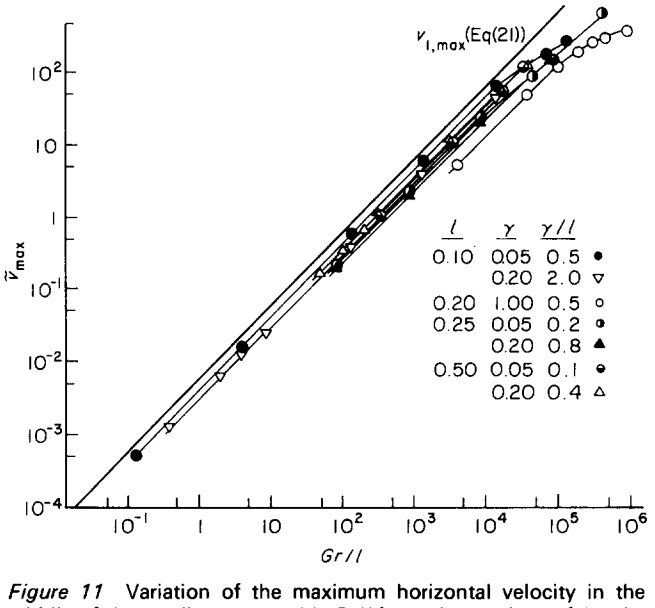

Figure 11 Variation of the maximum horizontal velocity in the middle of the gradient zone with Gr/l for various values of l and γ (analytical $\tilde{v}_{1,max}$ and computed solutions $\tilde{v}_{max,c}$ for $\gamma/l<1$ and $\gamma/l=2$ and 5)

(i) $\beta\approx 1$ when $\gamma\geqslant 0.20$ and $l\leqslant 0.15$;
(ii) $\beta\approx 0.37\exp(\gamma)$ when $\gamma\geqslant 0.20$ and $0.50\geqslant l\geqslant 0.25$;
(iii) $\beta\approx 0.43$ when $\gamma\leqslant 0.20$ and $0.50\geqslant l\geqslant 0.25$;
(iv) $\beta\approx 0.17\exp(1.2\gamma)$ when $\gamma<0.20$ and $l\leqslant 0.15$.

Over the range of γ and l considered, $\tilde{v}_{max,c}$ is always over-predicted by Eq (21); in the worst cases the difference $(1-\beta)$ is close to 60%.

Range of validity of functional laws for v_{max} at larger *Gr*

Influence of *Gr* on v_{max}

For different sets of values of l and γ, additional computations were made for a wide range of Gr, and the results for $\tilde{v}_{max,c}$ compared with the functional laws of Eqs (21) and (22). The results corresponding to $\gamma/l>1$ are plotted in Fig 10. Very good agreement was obtained for $l=0.1$ and $\gamma=0.2$ with the curve derived from Eq (22). For $\gamma=1$ and $l=0.2$ the computed results also fit very well the relation of Eq (22) up to $Gr/\gamma\approx 1.4\times 10^4$, where the transition to a boundary-layer-driven regime occurs, as revealed by the data's departure from linear variation in a way similar to that discussed by Bontoux *et al*[9].

The results concerning $\gamma/l<1$ are shown in Fig 11, with the previous results at $\gamma/l>1$ plotted as reference. The values of $\tilde{v}_{max}$ are plotted in terms of Gr/l. In accordance with Fig 9, the points are systematically under the curve corresponding to Eq (21). The velocity maximum $\tilde{v}_{max}$ is shown to be proportional to Gr/l at constant γ and l over a wide range of Gr/l. For Gr/l larger than 2×10^4 the data slightly vary from the linear curve, as in Fig 10, indicating the end of the conduction regime and the beginning of the boundary layer regime.

Influence of *Gr* on $(\partial\theta/\partial\tilde{y})_m$

When $\gamma=1$ the analytical relation of Eq (20) can be used even far from the beginning of the boundary layer regime but with adequate values of $(\partial\theta/\partial\tilde{y})_m$ given by functional laws[9].

The variation of $(\partial\theta/\partial\tilde{y})_m$ derived from computations when $\gamma/l<1$ is shown in Fig 12. As mentioned before, $l(\partial\theta/\partial\tilde{y})_m\approx 1$ for conducting regimes, but, when $Gr/l>7\times 10^3$, $(\partial\theta/\partial\tilde{y})_m$ is rapidly decreasing and becomes negative at $Gr/l\approx 3.6\times 10^4$ and 4.3×10^5, for $l=0.50$ and $l=0.25$, respectively. As a conclusion, the variation of $(\partial\theta/\partial\tilde{y})_m$ at large Gr and $l\geqslant 0.25$ is so strong that v_{max} cannot be directly connected to $(\partial\theta/\partial\tilde{y})_m$ as in Eq (20). However, the prediction still looks reasonable at $l=0.10$ and $\gamma=0.05$ when $Gr/l\approx 1.4\times 10^5$.

For $\gamma/l>1$, only two sets of values of γ and l have been considered (Fig 13). The results corresponding to $l=0.2$ and $\gamma=1$ indicate the end of the conduction regime at about $Gr/\gamma\geqslant 1.4\times 10^4$. Those for $l=0.1$ and $\gamma=0.2$ concern only conduction-dominated regimes up to $Gr/\gamma\approx 7\times 10^3$.

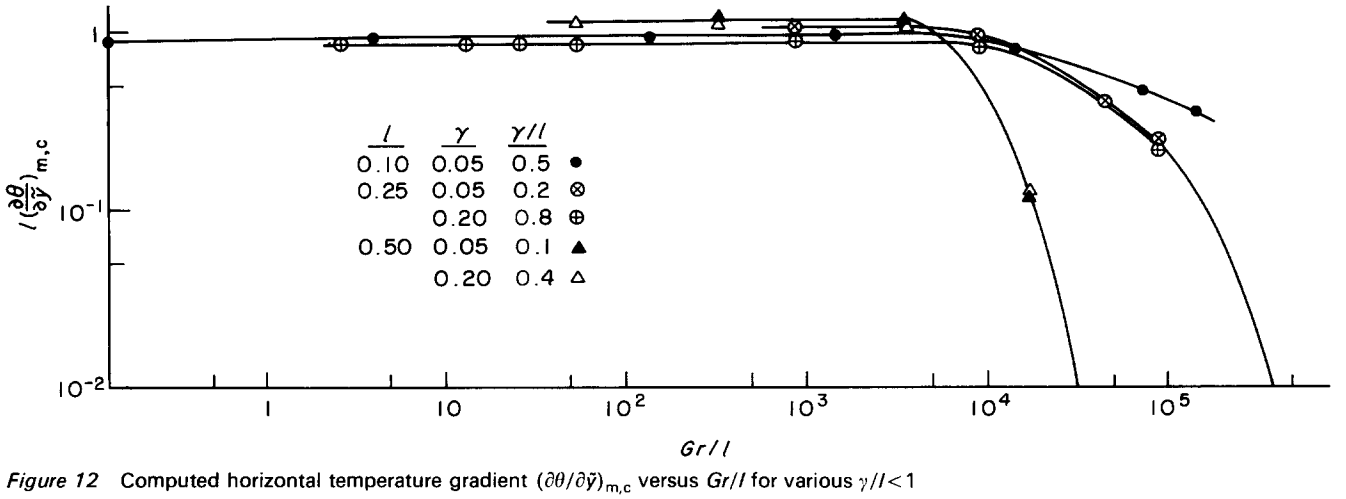

Figure 12 Computed horizontal temperature gradient $(\partial\theta/\partial\tilde{y})_{m,c}$ versus Gr/l for various $\gamma/l<1$

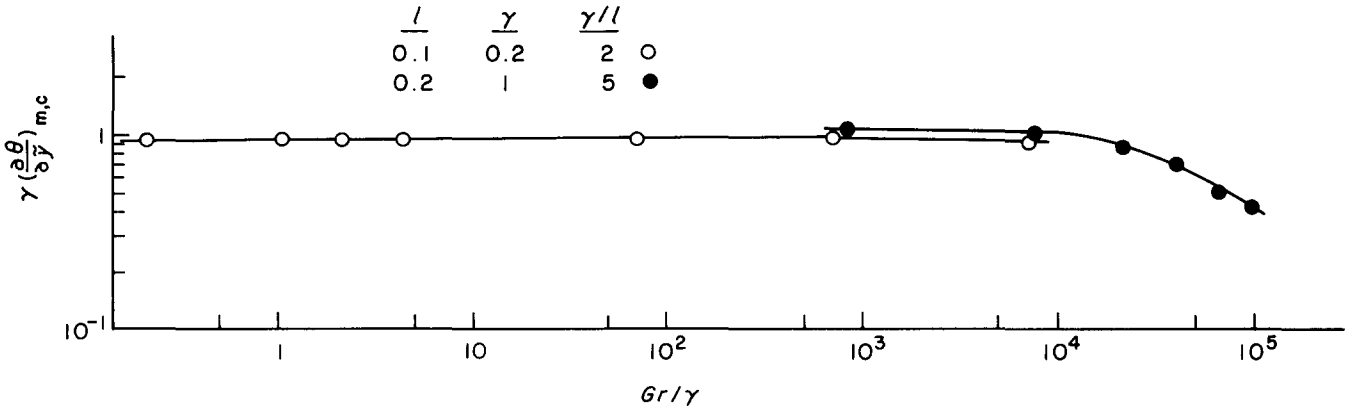

Figure 13 Computed horizontal temperature gradient $(\partial\theta/\partial\tilde{y})_{m,c}$ versus Gr/γ for various $\gamma/l>1$

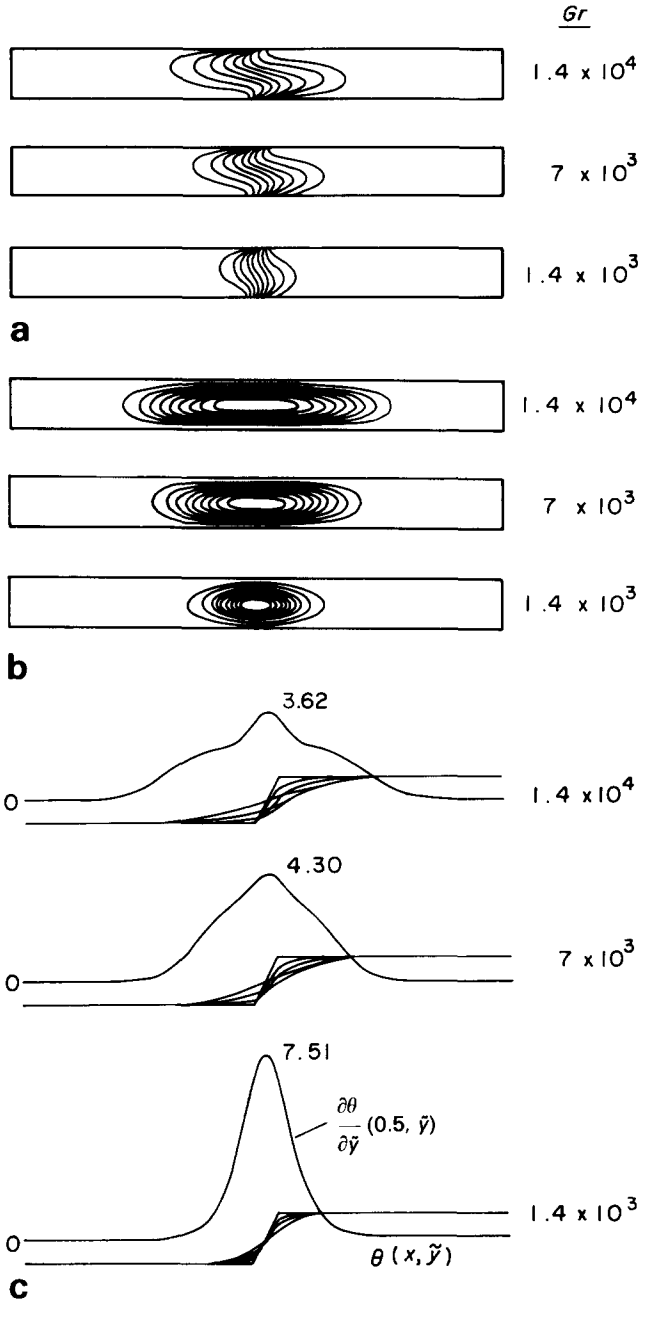

Figure 14 2Z model, $l=0.10$ and $\gamma=0.05$: (a) isotherm patterns; (b) streamline patterns; (c) temperature profiles $\theta(x,\tilde{y})$ at $x=0.0$, 0.1, 0.2, 0.3, 0.4, 0.5, and $\partial\theta/\partial\tilde{y}$ (0.5, $\tilde{y}$), for $Gr=1.4\times10^3$ ($\psi_{max}=-2.57$), 7×10^3 ($\psi_{max}=-7.02$) and 1.4×10^4 ($\psi_{max}=-10.17$)

Influence of *Gr* on dynamic and thermal patterns

The streamline and isotherm patterns are shown in Figs 14, 15 and 16 at $l=0.10$, 0.25 and 0.50, respectively, with $\gamma=0.05$. These graphs involve nine isolines such that $T_i=i-4/10$, with $i=0$ to 8, and $\psi_i=i/10\,\psi_{max}$, with $i=1$ to 9. The values of ψ_{max} are given in the figure captions. Horizontal profiles for the temperature and for its gradient (at the centre line) are also displayed for different values of Gr. The extrema of the gradient are given on the graphs.

The transition from the conduction-dominated regime to the boundary layer regime is mainly exhibited by the isotherm patterns. The onset of distortion in the isotherms, due to convection, occurs at $Gr/l\approx3600$, when $\gamma/l<1$ (Fig 12). When Gr is further increased, the isotherms are convected far away from the centre domain until they interact with the vertical walls (Fig 15(a)). In that case the buoyancy forces become important in the end regions. Over the range of Gr considered this confinement effect was not observed with $l=0.10$ and $\gamma=0.05$ (Fig 14(a)). With $l=0.25$ and 0.50, the confinement effect, which were arbitrarily characterized by $(\partial\theta/\partial\tilde{y})(x,\tilde{y})>0.1$ at $x=1/2$ and $y=0$, occurs respectively at $Gr\approx2\times10^4$ and 9×10^3. The critical value of Gr for the appearance of the confinement effect (following this criterion) seems to $Gr\approx4500/l$. Above the threshold, the isotherms tend to concentrate near the walls, and the core becomes almost isothermal ($\theta\approx0$) (Figs 15(a) and 16(a)). At the centre the isotherm $\theta=0$ can be strongly distorted at $Gr=1.1\times10^5$ for $l=0.25$ and at $Gr=1.7\times10^4$ with $l=0.50$ giving rise to the negative values of $(\partial\theta/\partial\tilde{y})_m$ mentioned above.

Although the modifications in the temperature profiles and the horizontal thermal gradient profiles are associated with the change in the flow structure, the streamline patterns look less disturbed for the range of parameters considered. When $l=0.50$ there is no obvious distortion in the pattern, except at $Gr\gtrsim8750$, where there is a slight increase of the flow parallelism in the middle of the cavity (Fig 16(b)). When $l=0.25$ the transition to the convection-dominated regime results in the vanishing of the 'cat-eye' pattern into a unicellular pattern which affects the entire cavity, with a regular parallel flow in the centre at $Gr=1.1\times10^5$ (Fig 15(b)). When $l=0.10$, the central basic cell spreads around the gradient zone with increasing Gr (Fig 14(b)). However, at the largest Gr value considered, $Gr=1.4\times10^4$, the confinement still does not limit the displacement of the isotherms.

Additional sets of streamline and isotherm patterns are given for $l=0.25$ and 0.50, with $\gamma=0.20$, in Figs 17 and 18. They confirm the previous observations made for $\gamma=0.05$, showing the effect of Gr, which is only slight on the streamlines but very strong on the isotherms for $2.2\times10^2\lesssim Gr\lesssim2.2\times10^4$ at $l=0.25$, and $1.75\times10^3\lesssim Gr\lesssim1.75\times10^4$ at $l=0.5$.

The comparison of the corresponding graphs, mainly in Figs 16 and 18 shows, that γ has only a small effect, at least in the range $0.05\leqslant\gamma\leqslant0.2$, when $\gamma\leqslant l$.

For $\gamma>l$, most of the conclusions of previous studies at $\gamma=1$

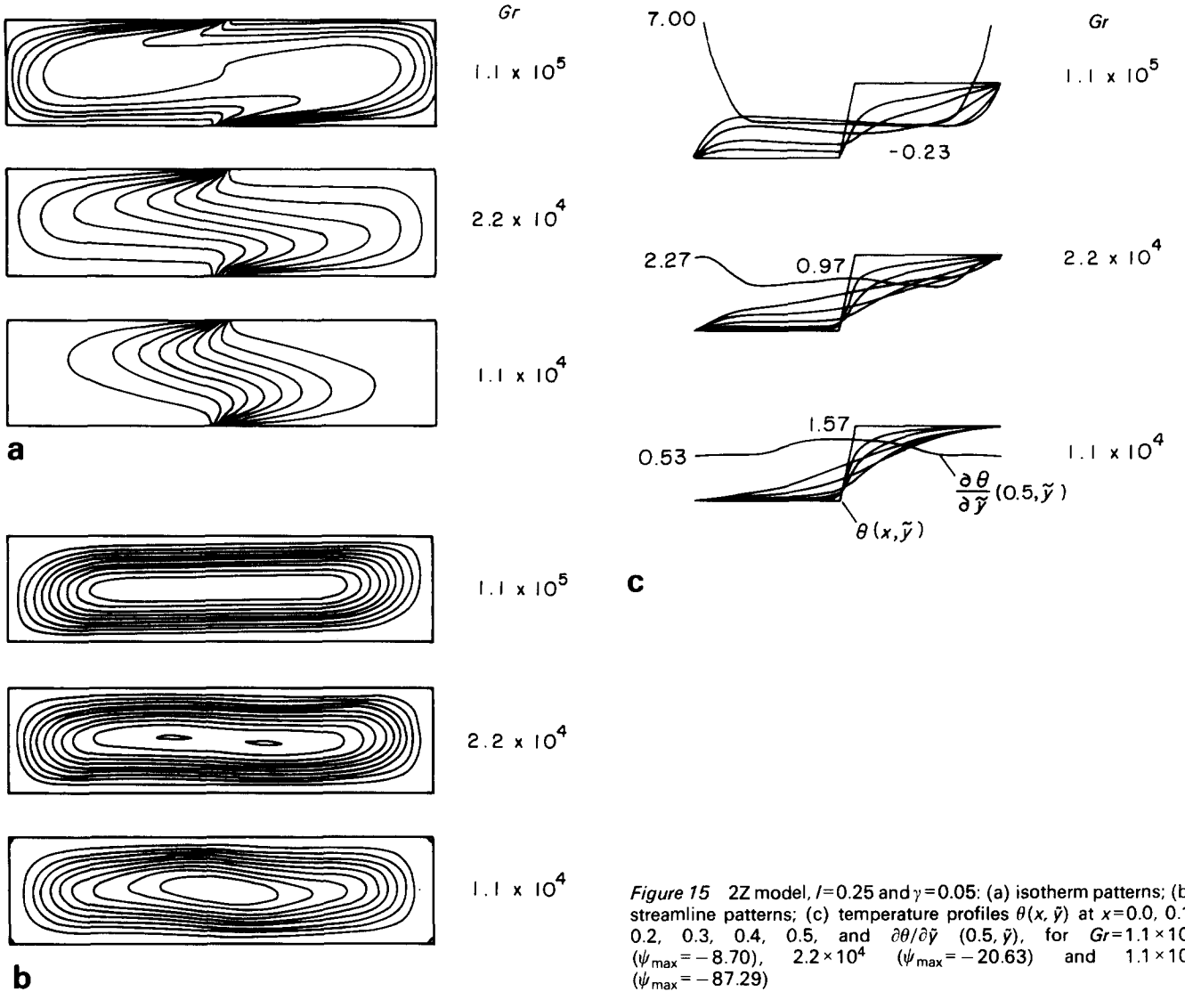

Figure 15 2Z model, $l=0.25$ and $\gamma=0.05$: (a) isotherm patterns; (b) streamline patterns; (c) temperature profiles $\theta(x, \tilde{y})$ at $x=0.0$, 0.1, 0.2, 0.3, 0.4, 0.5, and $\partial\theta/\partial\tilde{y}$ (0.5, $\tilde{y}$), for $Gr=1.1\times10^4$ ($\psi_{max}=-8.70$), 2.2×10^4 ($\psi_{max}=-20.63$) and 1.1×10^5 ($\psi_{max}=-87.29$)

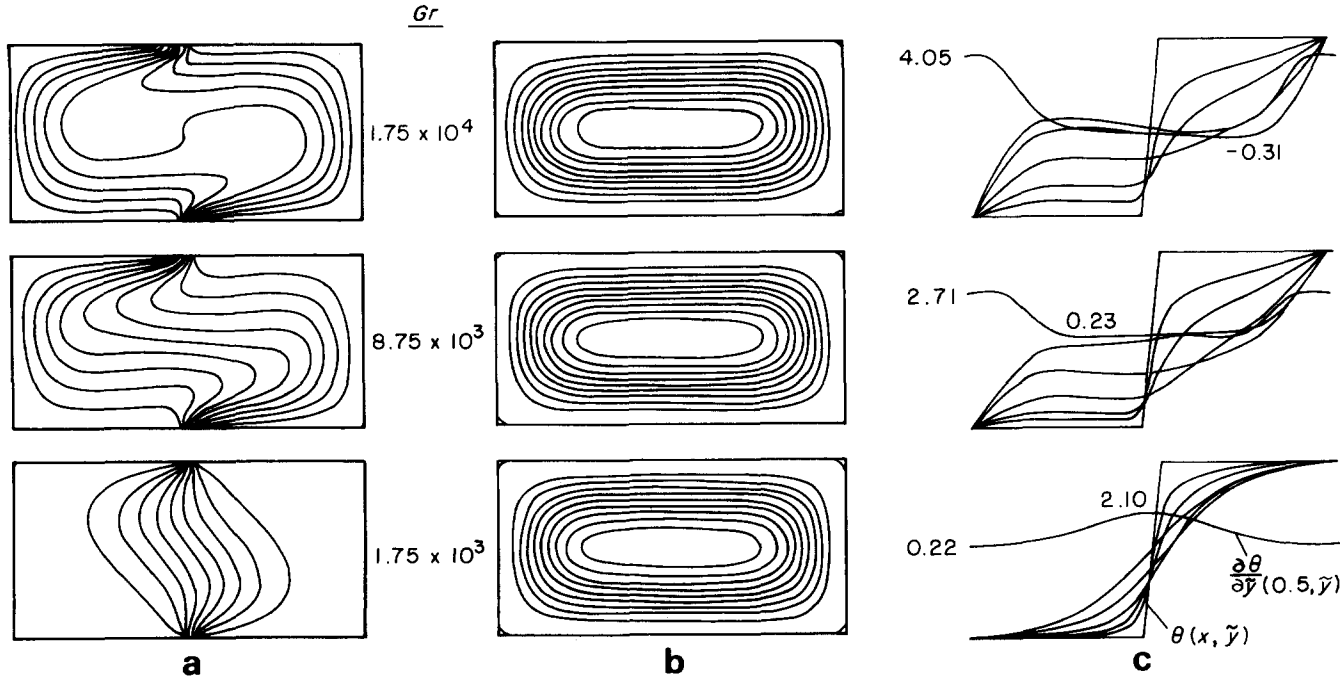

Figure 16 2Z model, $l=0.50$ and $\gamma=0.05$: (a) isotherm patterns; (b) streamline patterns; (c) temperature profiles $\theta(x, \tilde{y})$ at $x=0.0$, 0.1, 0.2, 0.3, 0.4, 0.5, and $\partial\theta/\partial\tilde{y}$ (0.5, $\tilde{y}$), for $Gr=1.75\times10^3$ ($\psi_{max}=-2.29$), 8.75×10^3 ($\psi_{max}=-11.27$) and 1.75×10^4 $\psi_{max}=-22.25$)

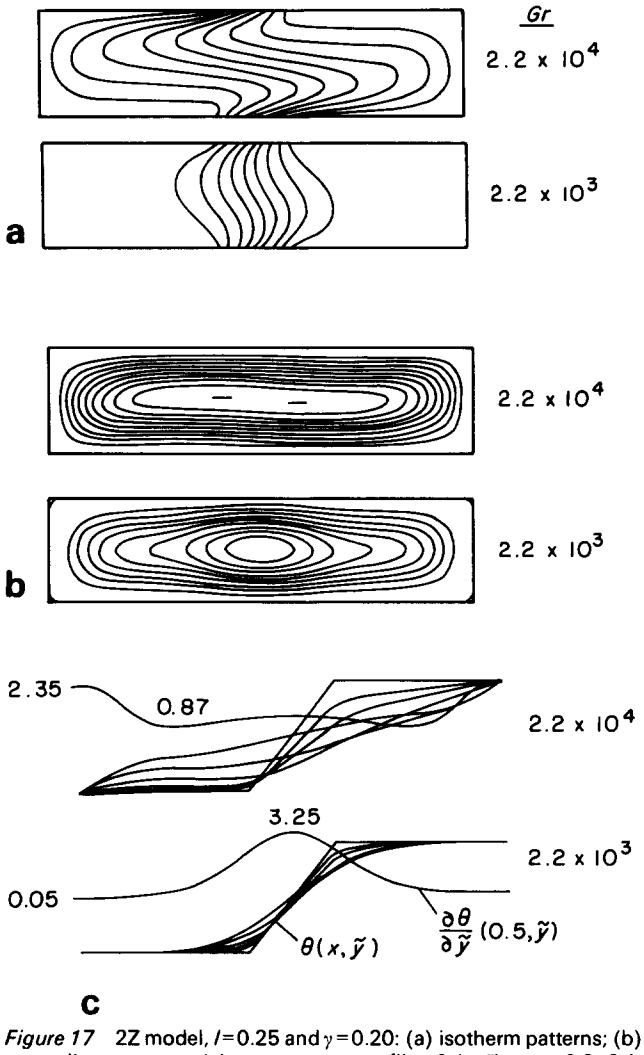

Figure 17 2Z model, $l=0.25$ and $\gamma=0.20$: (a) isotherm patterns; (b) streamline patterns; (c) temperature profiles θ $(x, \tilde{y})$ at $x=0.0$, 0.1, 0.2, 0.3, 0.4, 0.5, and $\partial\theta/\partial\tilde{y}$ $(0.5, \tilde{y})$, $Gr=2.2\times10^3$ ($\psi_{max}=-2.01$) and 2.2×10^4 ($\psi_{max}=-14.36$)

apply. The characteristic variable v_{max} increases linearly with $1/\gamma$ (Eq (22)).

For $\gamma<l$ the correlation for v_{max} is not so good even in the core-driven regime. Eq (21), based on $(\partial\theta/\partial y)_m$ overpredicts significantly the computed values of $v_{max,c}$. A correction parameter $\beta=\tilde{v}_{max,c}/\tilde{v}_{max}$ is given in terms of γ at various values of l in Fig 9.

Conclusions

The two-dimensional Boussinesq equations in rectangular cavities were solved numerically by an accurate finite difference technique. We considered the case where the buoyancy driving forces are generated by an external temperature gradient applied only on a given distance along the horizontal walls of the cavity. Such a situation corresponds, for instance, to a two-zone furnace for crystal growth processing by vapour transport.

An insight was obtained into the influence of the width, γ, of this external temperature gradient on the isotherm and streamline patterns for aspect ratios $0.10<l<0.50$ and for various Grashof numbers in a range including 'conduction' (or core-driven) intermediate and boundary layer regimes.

One of the goals of this study was to analyse the behaviour of $(\partial\theta/\partial\tilde{y})_m$, which is known in the classical limiting case of $\gamma=1$ and $l\to0$ to have a dominant influence on the maximum horizontal velocity v_{max} for the conducting and intermediate regimes. It was found that, for $0\leqslant\gamma\leqslant1$, $(\partial\theta/\partial\tilde{y})_m$ behaves like $1/l$ for $\gamma<l$ and like $1/\gamma$ for $\gamma>l$ in the core-driven regime.

The variation of the ration $\beta=\tilde{v}_{max,c}/\tilde{v}_{max}$ allows rapid prediction of $\tilde{v}_{max}$ accurate enough for practical applications, for example in crystal processing.

For the intermediate and boundary layer regime, the parameter $(\partial\theta/\partial\tilde{y})_m$ appears to become rapidly irrelevant, when Gr is increased, for a correct estimation of $\tilde{v}_{max}$, at least when $\gamma<l$. In that case only a direct numerical simulation, like the one shown in this paper, can give the correct evaluation of the flow field pattern.

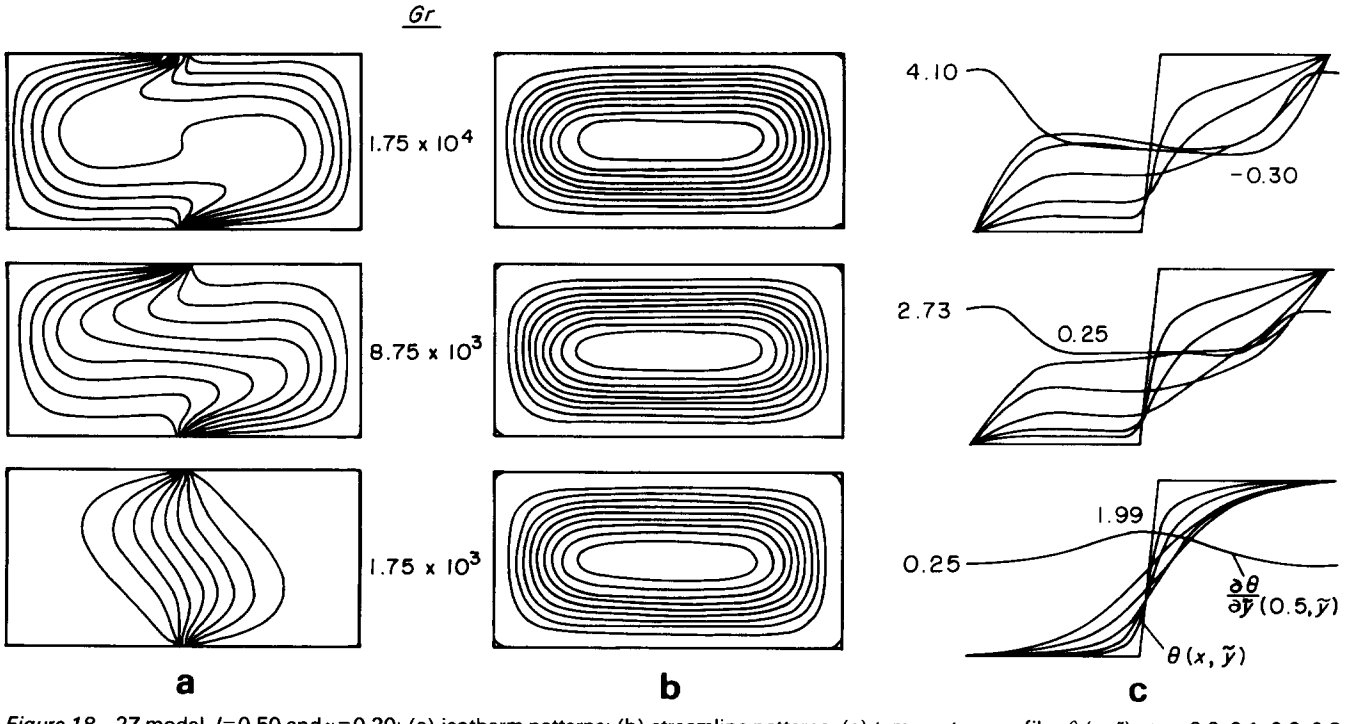

Figure 18 2Z model, $l=0.50$ and $\gamma=0.20$: (a) isotherm patterns; (b) streamline patterns; (c) temperature profiles θ $(x, \tilde{y})$ at $x=0.0$, 0.1, 0.2, 0.3, 0.4, 0.5, and $\partial\theta/\partial\tilde{y}$ $(0.5\,\tilde{y})$, for $Gr=1.75\times10^3$ ($\psi_{max}=-2.27$), 8.75×10^3 ($\psi_{max}=-11.25$) and 1.75×10^4 ($\psi_{max}=-22.22$)

Acknowledgements

Financial support by the DRET (Direction des Recherches et Etudes Techniques, Groupe 6) and CNES (Centre National d'Etudes Spatiales, Division des Programmes Scientifiques 'Matériaux') is acknowledged. Support for computations on Cray-1/S by the CCVR (Centre de Calcul Vectoriel pour la Recherche, Palaiseau), on IBM-3081 by the CNUSC (Centre National Universitaire Sud de Calcul, Montpellier) and the PA-Saint-Charles (Point d'Accès Informatique, Marseille) is also acknowledged.

The authors wish to thank Professor R. Cadoret and Dr J.-C. Launay for focusing their attention on heat and mass transfer problems involved in their crystal growth experiments.

References

1 Cormack, D. E., Leal, L. G. and Imberger, J. Natural convection in a shallow cavity with differentially heated end walls. Part 1: Asymptotic theory. *J. Fluid Mech.* 1974, **65**, 209–229

2 Pimputkar, S. M. and Ostrach, S. Convective effects in crystal growth from melt. *J. Cryst. Growth*, 1981, **55**, 614–646

3 Birikh, R. V. *J. Appl. Math. & Tech. Phys.*, 1966, **30**, 432

4 Hart, J. E. Stability of thin non-rotating Hadley circulations. *J. Atmos. Sci.* 1972, **29**, 687–697

5 Klosse, K. and Ullersma, P. Convection in a chemical vapour transport process. *J. Cryst. Growth*, 1973, **18**, 167–174

6 Bejan, A. and Tien, C. L. Fully developed natural counter-flow in a long horizontal pipe with different end temperatures. *Int. J. Heat Mass Transfer*, 1978, **21**, 701–708

7 Bejan, A. and Tien, C. L. Laminar natural convection heat transfer in a horizontal cavity with different end temperatures. *ASME J. Heat Transfer*, 1978, **100**, 641–647

8 Schiroky, G. H. and Rosenberger, F. Free convection of gases in a horizontal cylinder with differentially heated end walls. *Int. J. Heat Mass Transfer*, 1982, **27**, 103–110

9 Bontoux, P., Roux, B., Schiroky, G. H., Markham, B. L. and Rosenberger, F. Convection in the vertical midplane of a horizontal cylinder. Comparison of two-dimensional approximations with three-dimensional results. *Int. J. Heat Mass Transfer*, 1986, **29**(2), 227–240

10 Cormack, D. E., Leal, L. G. and Seinfeld, J. H. Natural convection in a shallow cavity with differentially heated end walls. Part 2: Numerical solutions. *J. Fluid Mech.*, 1974, **65**, 231–246

11 Imberger, J. Natural convection in a shallow cavity with differentially heated end walls. Part 3: Experimental results. *J. Fluid Mech.*, 1974, **65**, 247–260

12 Hart, J. E. Low Prandtl number convection between differentially heated end walls. *Int. J. Heat Mass Transfer*, 1983, **26**, 1069–1074

13 Hirsh, R. S. Higher order accurate difference solution of fluid mechanics problems by a compact differencing technique. *J. Comp. Phys.*, 1975, **10**, 90–109

14 Roux, B., Bontoux, P., Ta Phuoc Loc and Daube, O. Optimization of hermitian methods for Navier–Stokes equations in the vorticity and stream-function formulation. *Springer Verlag, L.N. in Math.*, 1980, **771**, 450–468

15 Roux, B., Grondin, J. C., Bontoux, P. and Gilly, B. On a higher order accurate method for the numerical study of natural convection in a vertical square cavity. *Numer. Heat Transfer*, 1978, **1**(2), 1–19

16 Mallinson, G. D. and De Vahl Davis, G. The method of false transient for the solution of coupled elliptic equations. *J. Comput. Phys.*, 1973, **12**, 435–461

17 Bontoux, P., Gilly, B. and Roux, B. Analysis of the effect of boundary conditions on numerical stability of solutions of Navier–Stokes equations. *J. Comput. Phys.*, 1980, **36**(3), 417–427

18 Farge, M. *Rapport SIMA No. HI/3912-00, EDF/DER*, Clamart, France, 1981

19 Gentzsch, W. Vectorization of computer programs with applications to computational fluid mechanics. *Vieweg Verlag Notes in Numerical Fluid Mechanics*, **8**, 1984

20 Manouélian, D. *Convection Thermique et Solutale dans une Enceinte Fermée. Application à l'Etude Hydrodynamique de la Croissance Cristalline en Phase Vapeur. Conservatoire Nat. des Arts et Métiers, Mémoire*, Aix-en-Provence, France, 1982